

1 Millikelvin-precision temperature sensing for advanced
2 cryogenic detectors

3 M. Antonova^a, J. Capó^a, A. Cervera^a, P. Fernández^{a,2}, M. Á. García-Peris^{a,1,*}, X.
4 Pons^b

^a*Instituto de Fisica Corpuscular Catedratico Jose Beltran 2 E-46980 Paterna (Valencia) Spain*

^b*CERN Espl. des Particules 1 1211 Meyrin Switzerland*

5 **Abstract**

Precise temperature monitoring —to the level of a few milli-Kelvin— is crucial for the operation of large-scale cryostats requiring a recirculation system. In particular, the performance of Liquid Argon Time Projection Chambers —such as those planned for the DUNE experiment— heavily relies on proper argon purification and mixing, which can be characterized by a sufficiently dense grid of high-precision temperature probes. In this article, a novel technique for the cross-calibration of Resistance Temperature Detectors (RTDs) in cryogenic liquids (argon and nitrogen) is presented, obtaining an unprecedented precision of 2.5 mK.

6 *Keywords:* Detectors, Liquid Argon, Cryogenics, Temperature, RTD, Purity,
7 Computational Fluid Dynamics

8 **1. Introduction**

9 Precise temperature sensing is essential in large cryogenic detectors, where the circulation
10 and purification of cryogenic liquids significantly impact overall detector performance.
11 Uncontrolled temperature gradients in such systems can disrupt the cryostat dynamics
12 and ultimately affect the experiment's physics sensitivity. In this work, we present the
13 calibration procedure of a novel temperature monitoring system developed for a prototype
14 of the future DUNE experiment.

*Corresponding author

Email address: miguel.garcia-peris@manchester.ac.uk (M. Á. García-Peris)

¹now in the University of Manchester

²now at Donostia International Physics Center, DIPC

DUNE, which stands for Deep Underground Neutrino Experiment [2], is expected to begin taking data toward the end of the decade. It aims to perform comprehensive neutrino oscillation analyses —broadly exploring the Charge-Parity (CP) violation parameters phase-space and resolving the neutrino-mass hierarchy problem [6]. Its extensive physics program also includes searches for hypothetical proton decay channels [3], multi-messenger astronomy from supernovae and neutrino bursts [8], and explorations of Beyond the Standard Model (BSM) physics [7]. Utilizing the most powerful neutrino beam ever constructed, generated at Fermilab, the experiment adopts a long-baseline neutrino oscillation approach with two detectors. The Near Detector, also at Fermilab, will characterize the unoscillated neutrino beam. The Far Detector (FD), located in the Sandford Underground Research Facility (SURF), 1300 km away from the ND and 1.5 km underground, will measure the oscillated flux.

In the Phase I, DUNE Far Detector will consist of two Liquid Argon Time Projection Chambers (LArTPCs) and is anticipated to begin operations by 2029. DUNE phase II will complement with two more modules by mid 30's, aiming at a total fiducial mass of 40 kilotonnes. The detector technology has been established, with excellent tracking and calorimetric capabilities, in several smaller-scale experiments [10, 13]. The first demonstration of the technology at the kilotonne scale has been carried out at the CERN Neutrino Platform as part of the ProtoDUNE program. In particular, the ProtoDUNE Single-Phase (SP) experiment [1] replicated the components of the DUNE FD Horizontal Drift (HD) [4] configuration at a scale 1:1, using a total argon mass 20 times smaller (770 tonnes). It was operated from mid-2018 to mid-2020, constituting the largest monolithic LArTPC to ever constructed and operated up to date [5, 9].

During ProtoDUNE-SP operation, the level of impurities was kept way below 100 ppt oxygen equivalent using a cryogenic recirculation and purification system [1, 9]. This is critical in an LArTPC, as the 3D images generated by charged particles traversing the detector can be significantly degraded by impurities in the medium—such as nitrogen, oxygen, and water—which absorb ionization electrons, thereby deteriorating spatial resolution and introducing biases in energy measurements. Three purity monitors, based on the ICARUS design [25], were installed outside the active volume of the TPC to measure the electron lifetime, which is inversely related to the residual concentration of

46 impurities. They ran twice a day to monitor the argon purity and thus to provide the
47 necessary corrections for posterior data analysis.

48 Achieving the necessary argon purity has been possible thanks to the studies based
49 on computational fluid dynamic (CFD) simulations, and the experience gained with
50 previous LArTPC demonstrators such as LAPD [11] and the 35-tonne prototype [12, 18],
51 which have paved the way to operate large-scale cryostats requiring low concentrations
52 of impurities. These studies have also shown that it exists a strong correlation between
53 temperature and purity in the liquid argon volume. The distribution of impurities is
54 insensitive to small ($\mathcal{O} \sim 1$ K) absolute temperature variations, but strongly depends on
55 the relative vertical temperature gradient. Since the bulk volume in the cryostats must
56 be continuously mixed with the incoming purified argon to ensure uniform purification
57 of the entire LAr volume, the temperature distribution serves as a clear indicator of
58 the mixing process: a homogeneous temperature distribution suggests proper mixing,
59 while large temperature gradients signal inadequate mixing. If the LAr bulk volume is
60 not mixed appropriately, a stratification regime can develop: a significant portion of the
61 liquid remains unpurified, generating ‘dead’ regions inside the detector. Thus, continuous
62 monitoring of this temperature gradient can identify and mitigate potential failures of
63 the purification system. In ProtoDUNE-SP, this gradient was predicted to be about 15
64 mK by the CFD simulations [1, 4].

65 Even with homogeneous mixing, the CFD simulations predict that the concentration
66 of impurities may vary across the cryostat volume, requiring a position-dependent correc-
67 tion to the electron lifetime. The Purity Monitors themselves are intrusive objects which
68 cannot be deployed inside the active volume, but rather only at a few well-defined loca-
69 tions near the cryostat walls; thus, precise inference of the electron lifetime map requires
70 alternative methods, as the one proposed in this article. A net of temperature sensors
71 cross-calibrated to the <5 mK level should allow the measurement of a 15 mK tempera-
72 ture gradient, which can be used to constrain CFD simulations, providing a data-driven
73 prediction of the impurity concentration. The main limitations of this new approach are
74 the precision of the cross-calibration of the temperature sensors and the accuracy of the
75 simulations. In this article, precise temperature monitoring for ProtoDUNE-SP will be
76 described, with particular emphasis on sensor calibration in the laboratory.

77 **2. The temperature monitoring system of ProtoDUNE-SP**

78 ProtoDUNE-SP [1] was the Single-Phase demonstrator of DUNE Far Detector HD mod-
79 ule [4]. The elements constituting the TPC, its associated readout electronics and the
80 photon detection system, were housed in a 8x8x8 m³ cryostat that contained the LAr that
81 served both as target and detector material. The cryostat, a free-standing steel-framed
82 vessel with an insulated double membrane, is based on the technology used for liquefied
83 natural gas storage and transport. A cryogenic system maintains the LAr at a stable
84 temperature of about 87 K by operating at a slight and constant over-pressure. It also
85 ensures the required purity level by means of a closed-loop process that recovers the evap-
86 orated argon, recondenses it, filters it, and recirculates it back into the cryostat, keeping
87 the LAr level at about 7.3 m from the bottom membrane. ProtoDUNE-SP was exposed
88 to a charged particle test-beam from October to November 2018, and later recorded cos-
89 mic rays until January 2020 [5, 9]. It was finally emptied and decommissioned during
90 Summer 2020.

91 In order to understand the LAr behaviour inside the cryostat and validate the CFD
92 simulations, 92 high-precision temperature sensors were installed inside ProtoDUNE-
93 SP, near the active volume. These sensors were distributed in two vertical arrays, or
94 Temperature Gradient Monitors (TGM), and two horizontal grids below and above the
95 TPC, respectively. Three elements were common to all systems: sensors, cables and
96 readout electronics. RTD technology [22] was chosen for this application. It consists of a
97 metallic element whose resistance changes with temperature. This resistance is measured
98 by feeding the RTD with a known current and measuring the resulting voltage. Based on
99 previous experience from other prototypes [12], Lake Shore PT102 platinum sensors [21]
100 with 100 Ω resistance at room temperature were chosen. Sensors were mounted on a
101 52x14 mm² PCB with an IDC-4 connector, such that they could be plugged-in at any
102 time. Several versions of the PCB have been explored, finally converging to the one
103 shown in Fig. 1, which minimizes the contact of the sensor with the PCB while keeping
104 the sensor protected.

105 A careful choice of the readout cable and the connections are essential to obtain the
106 required temperature precision. See for example Ref. [22] for a detailed description. A
107 custom cable made by Axon [14] was used. It consists of four American Wire Gauge

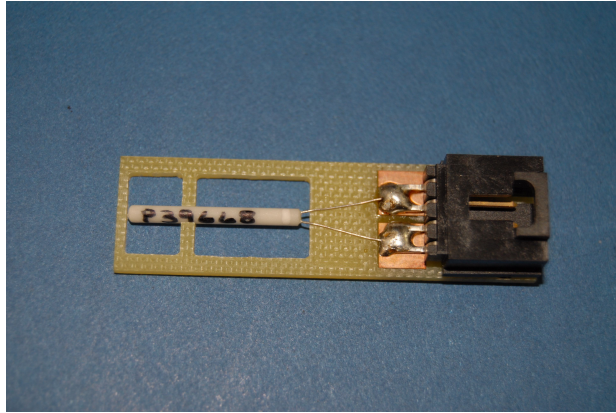


Figure 1: PCB support with temperature sensor and IDC-4 connector. The transition from two wires at the sensor to 4 wires at the readout is clearly seen. The sensor has a length of 2 cm.

108 (AWG) 28 teflon-jacketed copper wires, forming two twisted pairs, with a metallic ex-
109 ternal shield and an outer teflon jacket. The outer diameter of the cable is 3.7 mm.
110 Teflon was chosen for its good thermal properties and low out-gassing. The metallic
111 external shield (connected to the readout in one end and left floating at the sensor’s end)
112 and the twisted pairs are crucial to reduce the effect of external electromagnetic noise
113 pick-up. When RTDs are far from the voltmeter, the resistance of cables and connectors
114 are added to the one of the sensor, biasing the temperature measurement. This bias
115 can be subtracted to some level, but cannot be fully controlled since the resistance of
116 those elements also depends on temperature. To minimise the impact of this effect a four
117 wire-terminal readout is employed [22], such that the voltage is measured in the vicinity
118 of the RTD.

119 The last common element is the readout system, consisting of a very precise 1 mA
120 current source to excite the sensors and a 24 bits ADC to measure the voltage. The
121 readout system will be described in detail in Section 3.

122 As previously mentioned, ProtoDUNE-SP CFD simulations predict vertical tempera-
123 ture gradients as low as 15 mK [1]. A relative precision better than 5 mK was required to
124 validate and tune those simulations with sufficient confidence. Three main ingredients are
125 necessary to obtain such a precision: i) cryogenically rated, high-accuracy temperature
126 probes suitable for LAr applications., ii) a very precise readout system, and iii) accurate

127 and stable long-term calibration, both for the readout and the sensors. As mentioned
128 above, two TGMs were deployed in ProtoDUNE-SP: one could be moved vertically and
129 hence calibrated *in situ*, while the other one—static—fully relied on a prior calibration
130 in the laboratory. In this article, the calibration of the static TGM [17] sensors is de-
131 scribed in detail. This device consists of a vertical array of 48 sensors, installed 20 cm
132 away from the lateral field cage.

133 The calibration was performed once in spring 2018 (a few months before the operation
134 of ProtoDUNE-SP), and several times after ProtoDUNE-SP decommissioning. In this
135 article the calibration setup, procedure and results will be described in detail. Compar-
136 ison between the different calibration campaigns will be addressed, revealing important
137 information about systematic uncertainties and RTD ageing.

138 3. Readout system

139 A precise and stable electronic readout system is needed to achieve the required precision.
140 In previous versions of the calibration system, each sensor was connected to a different
141 and independent electronic circuit and thus, fed by a different current and read by a
142 different ADC channel. It was soon realized that the measured temperature difference
143 between any two pairs of sensors was heavily affected by the electronic offset between
144 channels. This offset was not constant, and showed dependence on ambient temperature
145 and humidity, which affected both the current source and the ADC, generating variations
146 of tens of mK for the measurement of a single calibration constant between two sensors.
147 A modified version of an existing PT100 mass temperature readout system, developed
148 at CERN for one of the LHC experiments [16], was adapted to address this issue. The
149 system consists of an electronic circuit that includes:

- 150 • A precise and accurate 1 mA current source for the excitation of the temperature
151 sensors based on an application of the Texas Instruments precise voltage reference
152 REF102CU with a possibility to adjust $\pm 10\text{nA}$ with Keithley 2001 multimeter [15,
153 23].
- 154 • A multiplexing circuit based on the Analog Devices ADG1407BRUZ multiplexer
155 with ultralow internal resistance in an 8-channel differential configuration. By in-
156 tegrating three multiplexers, the readout circuit supports simultaneous acquisition

157 from 24 channels. The multiplexing circuit and the current source are assembled
158 on a single card (see Fig. 2).

- 159
- 160 • A readout system based on National Instruments Compact RIO-FPGA device [19]
161 equipped with a NI-9238 analogue input module that provide 24 bits resolution over
162 1 volt range [20]. By programming the Van Dusen equation the readout calculates
163 the temperature in Kelvin units. The Compact RIO also drives the control bits of
the multiplexers

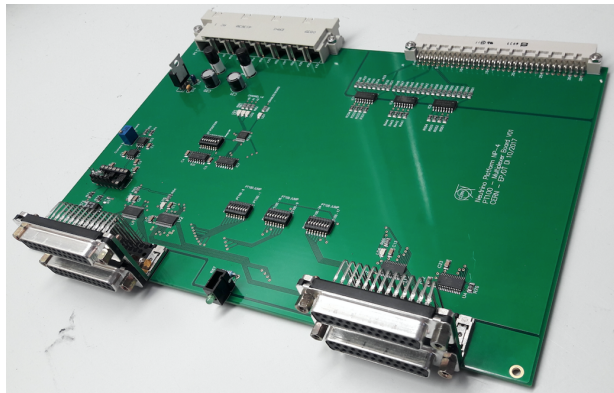


Figure 2: Current source and multiplexing card with 24 channels.

164 One of the features of the readout circuit is the serialization of the current source ex-
165 citation for all the sensors connected to the same board, such that the same current is
166 delivered to all of them. Multiplexing the signal of the sensors such that they can be
167 readout by the same ADC channel minimises the residual offset due to the electronics.
168 This system was used during the calibration campaigns presented in this article and also
169 for the temperature measurements during ProtoDUNE-SP operation.

170 The readout was not considered a potential source of bias during the calibration
171 campaign prior to the installation in ProtoDUNE-SP (see Sec. 4) and it was not studied
172 in detail at that time. However, in order to improve the calibration results following
173 ProtoDUNE-SP operation, a more detailed study of the readout system was conducted
174 prior to the calibration campaigns presented in 5. In particular, the twelve channels
175 (7-18) used for sensor calibration were investigated. It was found that, despite the use of
176 the multiplexing system, a small residual offset between channels persists. Fig. 3 shows

177 the offsets of channels 8-18 with respect to channel 7, computed using twelve 20-ohm
 178 precision resistors with a low Temperature Coefficient of Resistance (TCR)³ precision
 179 resistors, with an equivalent temperature of 76 K. Two of those, High Precision 1 (HP1)
 180 and High Precision 2 (HP2), are selected as the measurement samples and connected
 181 to the reference channel (7) and the channel being calibrated (from 8-18), while leaving
 182 all other channels connected to other secondary resistors to let the current flow through
 183 the system. The readout offset between channel 7 and channel X, $\Delta T_{7-X}^{readout}$, is then
 184 computed using the results of two consecutive measurements:

- 185 1. HP1 in channel 7 and HP2 in the channel X being calibrated. The offset between
 186 the measured temperatures is

$$\Delta T_{7-X}^A = T_X^{HP2} - T_7^{HP1} + \Delta T_{7-X}^{readout}. \quad (1)$$

- 187 2. HP2 channel 7 and HP1 in the channel X being calibrated. The offset between the
 188 measured temperatures is

$$\Delta T_{X-7}^B = T_X^{HP1} - T_7^{HP2} + \Delta T_{7-X}^{readout}. \quad (2)$$

189 Because of the very low TCR of the resistors, it can be assumed that the resistances
 190 are constants in these two measurements ($T_7^{HP1} = T_X^{HP1}$ and $T_7^{HP2} = T_X^{HP2}$). Thus,
 191 the offset between channels 7 and X can be computed as the average between those two
 192 measurements:

$$\Delta T_{7-X}^{readout} = \frac{\Delta T_{7-X}^A + \Delta T_{X-7}^B}{2}. \quad (3)$$

193 The results in Fig. 3, show an offset of up to 2.5 mK when comparing directly with
 194 channel 7, while the offset between any other two channels is below 1 mK, indicating
 195 a special feature of this channel. Error bars in that figure correspond to the standard
 196 deviation of four independent measurements (repeatability) of the same offset (see Fig. 3).
 197 As it can be observed the error is below 0.5 mK, what probes the great repeatability of

³The temperature coefficient of resistance is defined as the change in resistance per unit resistance per degree rise in temperature. Typically $\pm 5\text{ppm}/^\circ\text{C}$.

198 the readout. These offsets are more likely due to parasitic resistances in the different
 199 lines that are multiplexed. This finding allowed a correction to the measurements taken
 200 during the subsequent calibration campaigns, improving the obtained precision.

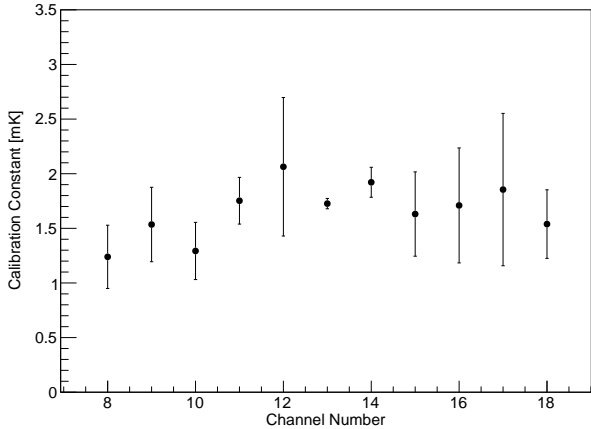


Figure 3: Offset between readout channels 8-18 and channel 7, used as reference. Points correspond to the mean of the 4 independent measurements and the error bars are their standard deviation.

201 4. Calibration before the installation in ProtoDUNE-SP

202 The Lake Shore Cryotronics company provides PT102 RTDs with a temperature ac-
 203 curacy of about 0.1 K, which is insufficient for ProtoDUNE-SP's requirements. While
 204 the company offers additional calibration to the 10 mK level, the cost is prohibitive.
 205 R&D on sensor calibration was identified as a crucial ingredient for the success of the
 206 ProtoDUNE-SP temperature monitoring system. For this particular application, sensor
 207 calibration consists in finding the temperature offset between any pair of sensors when
 208 exposing them to the same temperature. The experimental setup used for the calibra-
 209 tion of RTDs before their installation in ProtoDUNE-SP had two main components: i)
 210 the readout system used to monitor the sensor's temperature (described in the previous
 211 section) and ii) the cryogenics vessel and the associated mechanical elements used to
 212 put sensors together under stable and homogeneous cryogenics conditions. They were
 213 developed to achieve a relative calibration with a precision better than 5 mK.

214 *4.1. Experimental setup*

215 The mechanics of the calibration setup evolved significantly from the initial tests to the
216 final Static TGM calibration campaign. This evolution was primarily driven by the need
217 to improve offset stability and repeatability. The final configuration (see Fig. 4) consisted
218 of the following components:

- 219 • A polystyrene vessel formed by an outer box with dimensions $35 \times 35 \times 30 \text{ cm}^3$ and
220 4.5 cm thick walls, and a dedicated polystyrene cover, complemented by extruded
221 polystyrene panels glued into the inner walls and floor of the outer box, to conform
222 an inner empty volume of $10 \times 10 \times 20 \text{ cm}^3$.
- 223 • A $10 \times 10 \times 20 \text{ cm}^3$ 3D printed polylactic acid (PLA) box with two independent con-
224 centric volumes, placed in the inner volume of the polystyrene vessel. Its purpose
225 is twofold: i) to contain LAr, since polystyrene is porous to it, and ii) to create an
226 smaller inner volume with further insulation and less convection.
- 227 • A cylindrical aluminum capsule, to be placed in the inner volume of the PLA box,
228 with 5 cm diameter, 12 cm height and 1 mm thin walls. It had a circular aluminum
229 cover with a small opening to extract the cables and to allow LAr to penetrate
230 inside. The capsule was used to slowly bring sensors to cryogenic temperatures by
231 partial immersion in LAr with no liquid inside, minimizing thermal stress. Alu-
232 minum was chosen for its high thermal conductivity.
- 233 • A 3D printed PLA support for four sensors, to be placed inside the aluminum
234 capsule, keeping sensors always in the same position with respect to each other and
235 to the capsule walls.

236 The system described above ensures sufficiently stable and homogeneous conditions
237 within the inner volume, with three levels of insulation: the outer polystyrene vessel and
238 two PLA box LAr volumes. The aluminium capsule is key to this system and its usage
239 constituted a turning point in the R&D since it minimises thermal shocks, which were
240 identified as the main limiting factor for the repeatability of the sensor's offsets. Indeed,
241 variations of several tenths of mK were observed during initial tests without the capsule.
242 The problem was attributed to thermal shocks when, after many immersions in LN₂, one

²⁴³ of the sensors suffered a dramatic change in its offset (see Fig. 5). Examination at the
²⁴⁴ microscope revealed cracks in the outer RTD ceramics (see Fig. 6).



Figure 4: Final calibration setup. Left: polystyrene box with PLA box and aluminum capsule. Middle: aluminum capsule. Right: Sensor's support with four sensors.

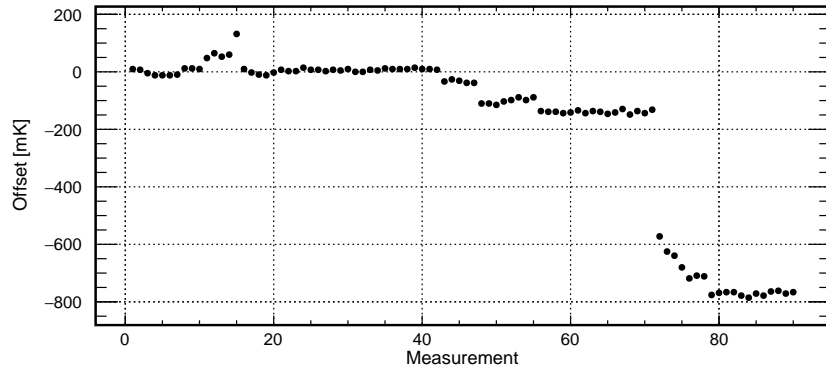


Figure 5: Offset between two sensors for 90 immersions in LN₂. A temperature drop of approximately 800 mK is observed around the 70th immersion point.

²⁴⁵ *4.2. Calibration procedure*

²⁴⁶ The calibration procedure relies on the assumption that all sensors in the capsule are at
²⁴⁷ the same temperature. This limits the number of RTDs in a single run to four, since
²⁴⁸ i) they should be as close as possible to each other and ii) as far as possible from the
²⁴⁹ capsule walls (the sensor closer to the wall could be biased). Two different methods,
²⁵⁰ described schematically in Fig. 7, were used to cross-calibrate all 48 sensors in runs of 4
²⁵¹ sensors:

²⁵² **1. Reference method:** all sensors are calibrated with respect to a reference one, in
²⁵³ sets of three sensors (the fourth one would be the reference sensor, which must be
²⁵⁴ present in all runs). In total there are sixteen calibration sets.

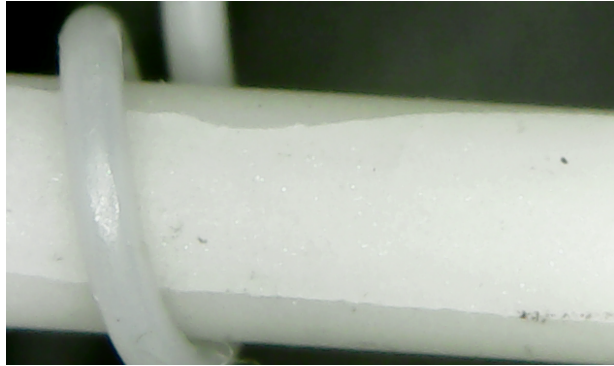


Figure 6: Cracks observed with the microscope in the ceramic of the sensor.

255 **2. Tree method:** Four different sets of sensors can be cross-calibrated by performing
 256 a second round of measurements with a single promoted sensor from each of those
 257 four sets. Since there are 16 sets in total, a third round of measurement is needed
 258 to cross-calibrate the four sets in the second round.

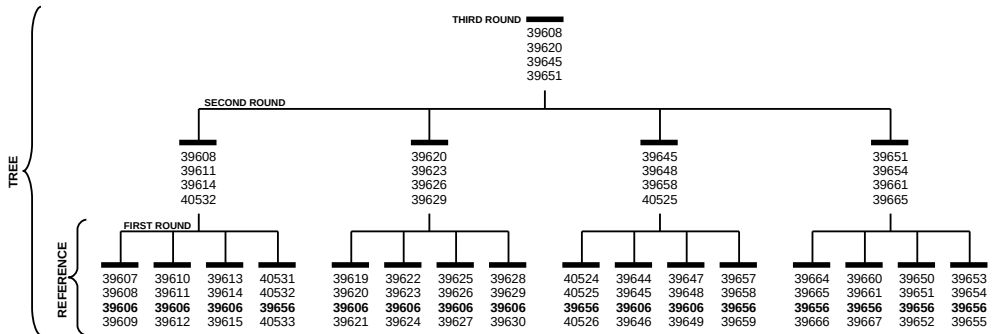


Figure 7: Schematic view of calibration sequence. Each number represents a different RTD, and the numbers in bold represent the reference sensors. The first round consists on a direct calibration respect to a reference sensor. The second and third rounds are needed to relate all sensors independently of the reference sensor.

259 The reference method was expected to be more precise since any two sensors were
 260 related through a single intermediate sensor (the reference one), while for the tree method
 261 the relation between any two sensors required more than one intermediate sensor. For
 262 example, the offset between sensors i and j in different sets, related through sensors k
 263 and l in the second round, would be $\Delta T_{ij} = \Delta T_{ik} + \Delta T_{kl} + \Delta T_{lj}$. For sensors related
 264 through the third round an additional term should be added, further increasing the offset

265 uncertainty.

266 Offset repeatability is a critical parameter to understand, as the laboratory calibration
267 must remain valid when applied to the actual detector. To study this, four independent
268 calibration runs were performed for each set of four sensors. However, due to concerns
269 about thermal fatigue in the primary reference sensor—subjected to 64 thermal cycles
270 over the four repeatability runs—three secondary reference sensors were employed to
271 regularly monitor its response and ensure reliability over time.

272 The following procedure is applied for each set of four sensors. First, they are placed
273 inside the aluminium capsule. The central connector closer to the red one is used for
274 the reference sensor. These positions are easily called by numbers from 1 (orange) to 4
275 (red), as shown in Fig. 8-left.

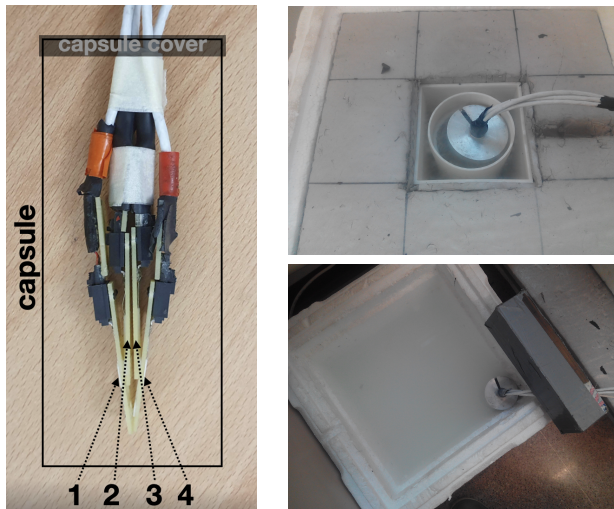


Figure 8: Left: Picture of sensor order inside the flask. Position 1 corresponds to highest serial number and 4 to lowest; position 3 is reserved to reference sensor. Top: Flask partially introduced in LAr. Bottom: Flask partially introduced in room water to warm up sensors before performing a new measurement.

276 After filling the PLA box with liquid argon, the aluminum capsule is partially im-
277 mersed (see Fig. 8-right-top), allowing the air inside to cool down gradually. This setup
278 prevents the sensors from coming into direct contact with liquid argon, instead inducing
279 a slow cooldown through the surrounding cold gas atmosphere, thereby avoiding thermal
280 shock. When the monitored temperature approaches the one of LAr (< 95 K), which
281 takes about 15 minutes, the capsule is completely immersed, being filled with liquid.

282 The PLA box is then completely filled with LAr to account for evaporation during the
283 cool-down phase. Finally, the polystyrene vessel is closed using the polystyrene lid. The
284 calibration run actually begins at that point and lasts for 40 minutes.

285 When the measurement is finished, the capsule is extracted from the liquid, emptied
286 of LAr and partially immersed into another polystyrene box filled with water at room
287 temperature (see Fig. 8-right-bottom). The warm-up process takes about ten minutes.
288 When sensors have reached a temperature around 250 K a new independent calibration
289 run can start.

290 Fig. 9 shows the typical evolution of the temperature for the four sensors in the
291 capsule during the warm-up and cool-down processes. A sudden fall to 87 K is observed
292 at minute 32, which corresponds to total immersion of the sensors in LAr. Notice also
293 that two of the sensors have lower temperature during the cool-down process; those are
294 sensors 1 and 4, the ones closer to the capsule walls.

295 For each set of sensors the procedure described above is repeated four times, resulting
296 in four independent measurements of the same offset. These measurements are used to
297 compute a mean offset value and its standard deviation (repeatability from now on).

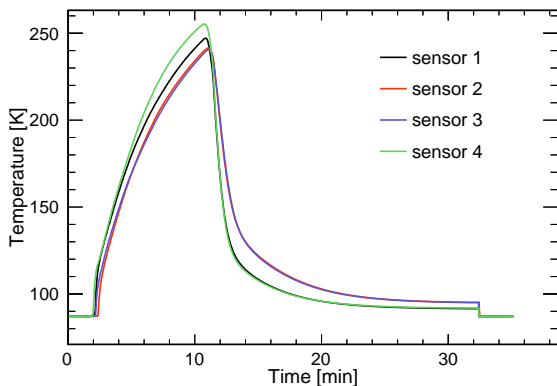


Figure 9: Temperature evolution between two calibration runs, showing the warm-up and cool-down phases of the four temperature sensors inside the capsule. Sensors 1 and 4 are located closest to the capsule walls.

298 *4.3. Calibration results*

299 Here we present the results of the calibration using both calibration methods, a study of
300 the consistency of these results, and a preliminary estimation of the systematic uncer-

301 tainty of the calibration process.

302 4.3.1. Results on the first round of measurements

303 Fig. 10 shows the offset of three different sensors with respect to the reference sensor as
304 a function of time, and for four independent calibration runs. The offset is more stable
305 for the sensor closer to the reference (position 2), while external sensors (positions 1
306 and 4) present larger variations, but show similar patterns between them. This effect
307 is attributed to the geometry of the system, with sensors at different heights and not
308 symmetrically positioned with respect to the capsule walls. This was taken into account
309 when developing the second version of the system, presented in Sec. 5.

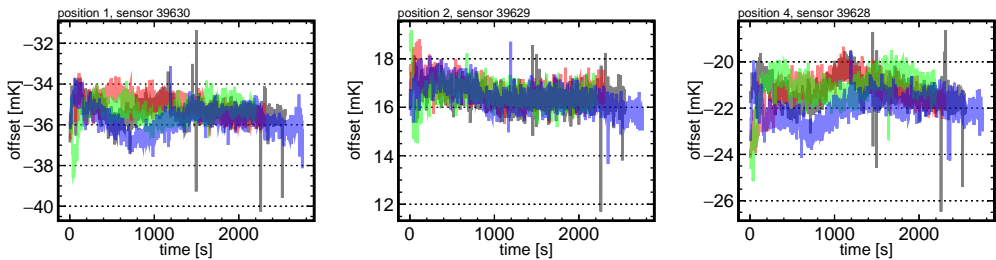


Figure 10: Offset between the reference sensor and each of the three sensors in a set, as a function of time. Each colour represents an independent calibration run.

310 The mean offset for each sensor and each calibration run is calculated as the average
311 over the time interval between 1000 and 2000 seconds, identified as the most stable region
312 for the majority of the runs. The standard deviation of the four means is taken as the
313 uncertainty, hereafter referred to as repeatability. As shown in Fig. 11, the uncertainties
314 are generally below 1 mK, demonstrating the high level of repeatability achieved in the
315 calibration process.

316 4.3.2. Time walk correction for reference sensors

317 Time evolution of the response of sensor 39606 was studied by periodically (every \sim 20
318 immersions) computing its offset with respect to three secondary reference sensors, 39603,
319 39604 and 39605. For each of those additional calibrations, two runs were taken instead
320 of four in order to minimize thermal fatigue of the reference sensor. As shown in Fig. 12-
321 left, the offset, computed as the mean of those two runs, varies linearly at a rate of
322 0.07 mK/immersion, which suddenly increases to 0.22 mK/immersion after 60 runs.

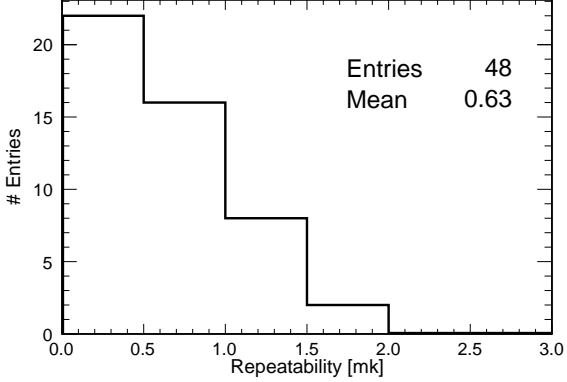


Figure 11: Distribution of the repeatability for calibration runs in the first round.

This change in the slope may be related with to the frequency of immersions, which increased from 3/day to 5/day. Sensor 39606 was initially used for other purposes, and the calibration of the 48 sensors conforming the static TGM started approximately at immersion 40. Given this change in its response, sensor 39606 was substituted by 39656 as primary reference for the last quarter of the TGM calibration in order to avoid further fatigue and potential untraceable behaviour. The evolution of the new reference sensor is shown in Fig. 12-right. It is worth noting that the same slopes are valid for the three secondary reference sensors in both cases, supporting the idea that the change observed in the offsets can be exclusively attributed to thermal fatigue of the reference sensor.

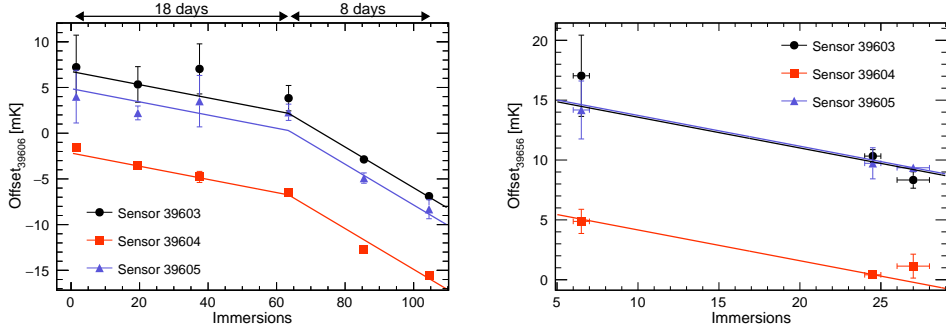


Figure 12: Offset between the reference sensors (39606 on the left panel and 39656 on the right panel) and the three secondary references as a function of the number of immersions. Offsets for sensor 39604 have smaller errors because of its position inside the capsule. Solid lines correspond to the parametrization in Eq. 4.

332 The zero intercept in both panels of Fig. 12 corresponds to the unbiased offset (or the
 333 offset at $N_{\text{immersions}} = 0$) of each of the secondary reference sensors with respect to the
 334 primary reference. In order to compute the unbiased offset for a sensor s , a time walk
 335 correction after N immersions is parameterised as:

$$\Delta T_{s,06}(N=0) = \begin{cases} \Delta T_{s,06}(N) + (0.072 \pm 0.003) * N & N < 63.5 \\ \Delta T_{s,06}(N) + (0.072 \pm 0.003) * 63.5 + \\ +(0.223 \pm 0.007) * (N - 63.5) & N > 63.5, \end{cases} \quad (4)$$

$$\Delta T_{s,56}(N=0) = \Delta T_{s,56}(N) + (0.168 \pm 0.007) * N. \quad (5)$$

336 All sensors can be related to the same primary reference sensor, 39606, adding the
 337 unbiased offset between sensors 39606 and 39656, $\Delta T_{56,06}(N=0)$, to sensors calibrated
 338 with respect to 39656. By averaging over the three secondary reference sensors, the value
 339 obtained is $\Delta T_{56,06}(N=0) = -9.19 \pm 0.13$ mK.

340 4.3.3. Results on the reference method

341 Fig. 13 shows the offset of all sensors with respect to the 39606 reference. As it can
 342 be noticed, the dispersion of the offsets is compatible with 0.1 K, the value quoted by
 343 the vendor. Fig. 14-left shows the distribution of the repeatability of the computed
 344 calibration constants after applying the different corrections, showing an average value
 345 below 1 mK.

346 4.3.4. Results on the tree method

347 The offsets are computed in this case with respect to an arbitrary reference among all
 348 sensors being calibrated. Selecting as reference a sensor present in the third round (see
 349 Fig. 7) minimizes the number of operations required to compute the offsets, thereby
 350 reducing the associated uncertainty. Sensor 39645 was chosen as reference. Fig. 14-right
 351 shows the distribution of the repeatability of the computed calibration constants, the
 352 mean of which is slightly below the one obtained for the reference method. Thus, it
 353 is confirmed that despite the higher number of intermediate sensors to relate any two
 354 sensors, the additional uncertainty introduced by the time walk correction makes the tree
 355 method superior to the reference method. Moreover, the reference method introduces a
 356 —not yet known— systematic error associated to the time wall correction model.

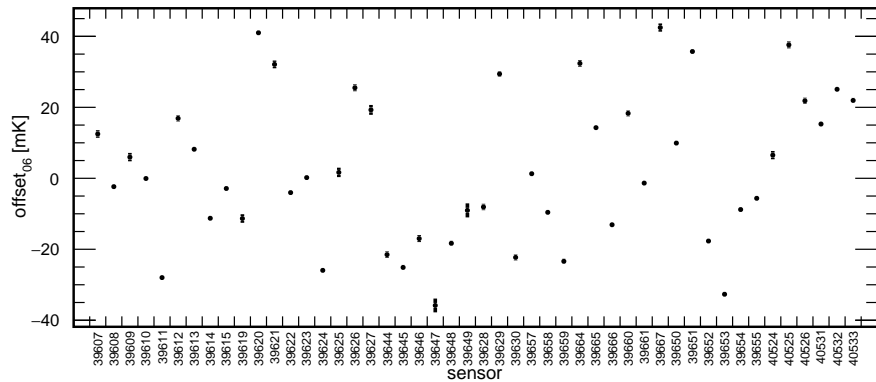


Figure 13: Offset of each sensor with respect to reference sensor 39606 using the reference method.

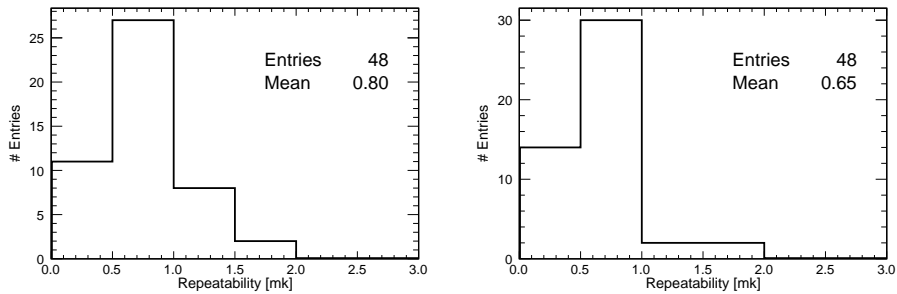


Figure 14: Left: repeatability distribution for the reference method. Right: repeatability distribution for tree method.

357 4.3.5. *Consistency cross-check and error estimation*

358 The uncertainties presented are, on average, smaller than 1 mK and correspond to the
359 standard deviation of the four independent measurements of each calibration constant,
360 combined with the error propagation from the required corrections: time-walk correction
361 for the reference method, addition of calibration constants for the tree method, and the
362 uncorrected electronic residual offset common to calibration methods. These corrections
363 likely include unknown systematic effects impacting the final calibration constants, which
364 need to be added to the systematic uncertainty associated to the assumption of homoge-
365 neous temperature inside the capsule. To estimate the overall precision of the calibration,
366 the following cross-check was performed. The calibration strategy yields two independent
367 values for each sensor's calibration constant—one obtained from the reference method
368 and the other from the tree method. For the sixteen sensors used in the second round of
369 the calibration tree, these two values are linearly independent because they are derived
370 from different sets: the reference method relies solely on first-round runs, while the tree
371 method uses only second and third-round runs for those sensors. Therefore, these sixteen
372 sensors provide an effective basis for estimating the calibration procedure's precision by
373 comparing the results obtained from the two methods.

374 By construction, the result of subtracting the calibration constants obtained in the
375 two methods should be compatible with the offset between sensors 39645 and 39606,
376 $\Delta T_{45,06} = \Delta T_{s,06} - \Delta T_{s,45} = T_{45} - T_{06}$, used as reference for the tree and reference
377 methods respectively. This offset is found to be -25.1 ± 0.7 mK by direct measurement
378 of the two sensors (see 10th column in Fig. 7 and 13). Fig. 15 shows this benchmark with
379 (left) and without (right) time walk corrections for the 16 sensors aforementioned, probing
380 the self-consistency of this correction. The standard deviation of this distribution, 2.4
381 mK, is an estimation of the quadratic sum of the total uncertainty of both calibrations.
382 Assuming that the reference sensor method has a larger uncertainty than the tree method
383 due to the time walk correction, an upper limit of 1.7 mK for the total error of the tree
384 method can be assumed. In the same way, this is the inferior limit for the total error of
385 the reference method. In both cases, these errors are less than half of what was originally
386 required for the temperature monitoring system in DUNE FD-HD.

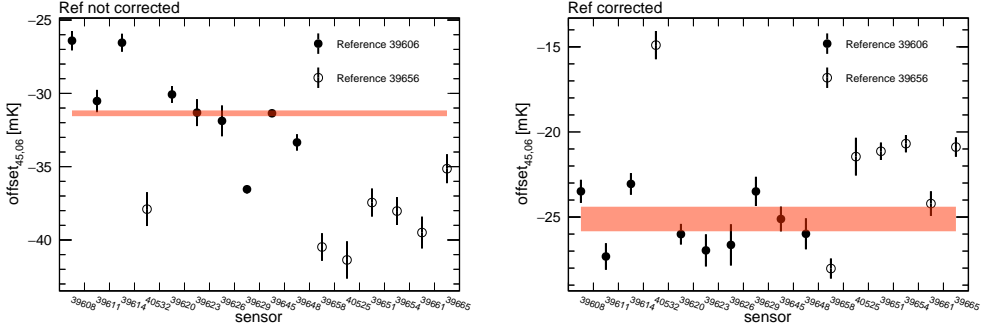


Figure 15: $\Delta T_{45,06}$ computed through all sensors of the second round of the calibration procedure. Left: not applying corrections. Right: applying corrections. A clear improvement is obtained using the corrections on the reference sensor. The red line represents the expected value of this calibration constant.

387 5. Re-calibration after ProtoDUNE-SP operation

388 After ProtoDUNE-SP decommissioning in 2020, temperature sensors were disconnected
 389 from the TGM and re-calibrated several times (see Table 1), using both LAr and LN2 as
 390 cryogenic liquid. The comparative analysis of those re-calibrations not only offers insights
 391 into the long-term stability of the sensors but also elucidates any potential dependencies
 392 on the choice of the cryogenic liquid. Although DUNE will use LAr, massive RTD
 393 calibration would benefit from using LN2, given its higher accessibility and lower cost.

Date	Cryogenic liquid	# Sensors in capsule
March 2018	LAr	4
February 2022	LN2	14
March 2023	LN2	14
July 2023	LAr	14

Table 1: Calibration runs with indication of the date, the cryogenic liquid used and the number of sensors inside the capsule.

394 In this section, a description of the setup used for these new calibrations, the changes
 395 applied to the procedure as well as the results and conclusions of these calibrations are
 396 presented.

397 5.1. Evolution of the calibration setup

398 The FD-HD module will be equipped with over 500 precision sensors [4], making the use
 399 of the current calibration setup impractical, as it can accommodate only four sensors

400 simultaneously. Significant modifications have been introduced in order to increase this
401 number to twelve, while maintaining the precision achieved during the 2018 calibration
402 campaign. This was accomplished by positioning sensors at the same height, to avoid
403 any potential vertical gradient, and following a cylindrical configuration, under the as-
404 sumption that convection inside the capsule has rotational symmetry. This symmetry
405 is also kept outside the capsule in all concentric cryogenic containers, having added a
406 fourth independent volume which should further reduce convection inside the inner cap-
407 sule. This notable advancement greatly streamlines the calibration process and serves
408 to reduce both statistical and systematic errors associated with the procedure. Fig. 16
409 shows the different elements of the new calibration setup, which are described below:

- 410 ● A polystyrene box with dimensions $55 \times 35 \times 30 \text{ cm}^3$ and 4.5 cm thick walls with
411 a dedicated cover of the same material.
- 412 ● Extruded polystyrene rectangles with a cylindrical hole of 12.5 cm diameter and
413 25 cm height, to conform the inner volume.
- 414 ● A PTFE container with 12.5 cm diameter, 25 cm height and 2 mm thick walls to
415 fit in the hole left in the box. The approximate volume is 2 L.
- 416 ● A 3D printed PLA cylinder with two independent concentric volumes, placed inside
417 the PTFE container.
- 418 ● A cylindrical aluminum capsule to be placed in the inner volume of the PLA cylin-
419 der. It has 7 cm diameter, 14 cm height and 1 mm thick walls.
- 420 ● A 3D printed PLA holder for 14 sensors, 12 of them forming a circle (the ‘corona’)
421 and the other 2 at the center, to be used as references. This support can be attached
422 to the aluminum capsule at a fixed height. Cables are naturally extracted from the
423 top of the assembly. A detailed view of this holder can be found in Fig. 16.
- 424 ● The readout electronics, described in Sec. 3 has been retained from the previous
425 setup.
- 426 ● A more cost effective cable with similar performance has been used. Produced by
427 Tempsons [24], it has four twisted cables instead of two separated twisted pairs

428 and an additional Kapton insulation layer between the shielding mesh and the four
429 conductors. Its diameter is 2.7 mm.



Figure 16: Left: The four concentric volumes of the calibration setup. Center: A view of one of the references and two corona sensors. Right: The 12 corona sensors plus the 2 references.

430 *5.2. Calibration procedure*

431 The sensor support was originally designed to accommodate two reference sensors in
432 the center (see Fig. 16), enabling both the reference and tree calibration methods.
433 However, it was soon observed that temperature variations between corona and reference
434 sensors were significantly larger than those between any two corona sensors. This effect
435 is attributed to the convection pattern inside the capsule, which is expected to have
436 rotational invariance, and hence favour sensors disposed following a cylindrical symmetry.
437 This can be observed in Fig. 17-left, where the offset between two corona sensors is
438 nearly constant in time in four independent measurements, and in Fig. 17-right, where
439 the offset between a corona and a reference sensor shows a more chaotic behaviour.
440 Consequently, only the ‘tree’ calibration method was considered during the calibrations
441 after ProtoDUNE-SP decommissioning.

442 The new calibration tree, shown in Fig. 18, contemplates four 12-sensors sets in the
443 first round, and a unique second round with three promoted sensors from each of the
444 sets in the first round. With this scheme, promoted sensors only suffer 8 baths, avoiding
445 the necessity of a time-walk correction.

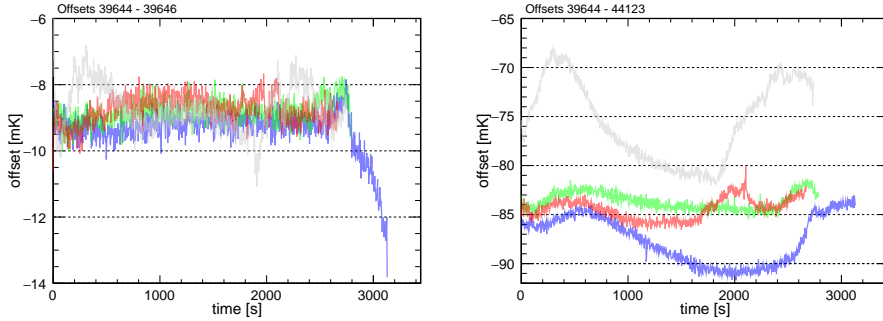


Figure 17: Left: The 4 measured offsets between two arbitrary sensors in the corona. Right: The 4 measured offsets between a sensor in the corona and one of the references, at the center.

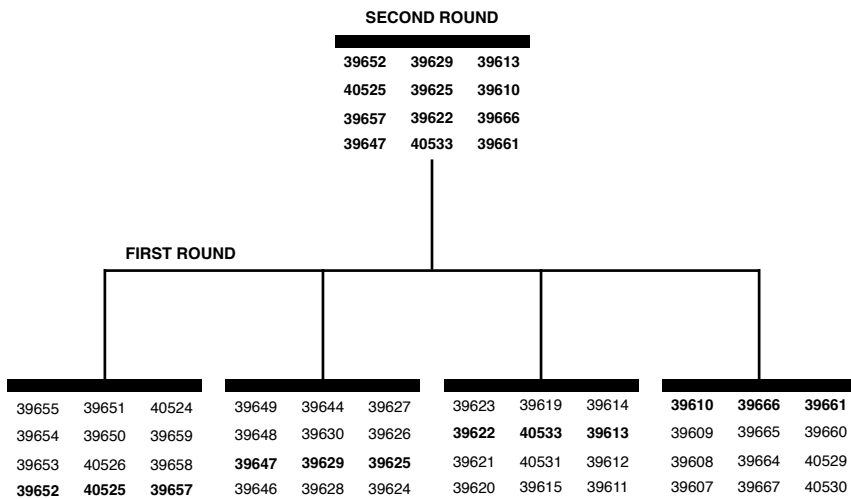


Figure 18: Schematic of the calibration sequence used with the new setup. Each of the sets contains 12 sensors, all of them placed in the corona, plus 2 references at the center. Sensors in bold in the first round are promoted to the second round.

446 The experimental procedure is similar to the one presented in Sec. 4. Two small
447 variations were introduced. First, the several concentric containers are cooled down
448 for 40 minutes before introducing the aluminium capsule for the first time in a day,
449 slightly improving the results of the first calibration run. Second, the warm up process
450 is accelerated using a heat gun, avoiding the use of water.

451 *5.3. Calibration results*

452 A sensor from the second round is chosen as the reference, as this minimizes the number of
453 operations required for the non-promoted sensors. Since each set includes three promoted
454 sensors, there are three **linearly independent** ways to compute the offset relative to the
455 reference for the nine non-promoted sensors in that set. The calibration constant for these
456 sensors is calculated as the weighted average of the three “paths”, with its uncertainty
457 given by the standard deviation of these three values. The offset uncertainty used in the
458 weighted average for each of the three paths is computed by quadratically summing the
459 individual uncertainties (as in Fig. 19) of all terms contributing to the offset along that
460 specific path. Sensor 40525 is adopted as the reference for the remainder of the analysis.

461 Fig. 19 shows the distribution of the repeatability (defined in Sec. 4.3.1) for the three
462 new calibrations mentioned in Table 1. **AÑADIR AQUÍ EL PORQUÉ LAR2023 TIENE**
463 **47 entries.** In all three cases the uncertainty is slightly above 1 mK. Mean values are
464 larger than the ones obtained in the 2018 calibration campaign. This is attributed to
465 the increased capsule size and the larger distance between sensors inside the capsule.
466 This hypothesis is supported by Fig. 20, showing the repeatability as a function of the
467 distance to the reference sensor in the corona for a particular measurement. However,
468 there is no substantial difference between the repeatability obtained for LN2 and LAr
469 calibrations.

470 Comparison between LN2 and LAr calibrations can also be used to understand the
471 dependence of the calibration constants on the absolute temperature. This is shown
472 in Fig. 21 along with other comparisons between calibration campaigns. The standard
473 deviation of the distribution is lower when comparing two calibrations in the same liquid
474 (LN2 in this case). However no bias is observed when comparing calibrations in two
475 different liquids, indicating that offsets are insensitive to a 10 K variation in absolute
476 temperature.

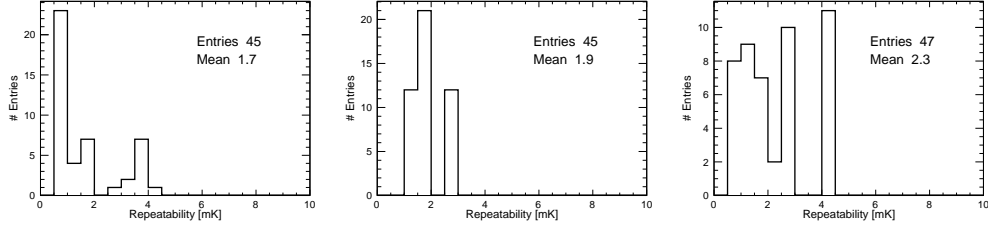


Figure 19: Repeatability distribution for the new calibrations. Left: LN2-2022. Middle: LN2-2023, Right:LAr-2023

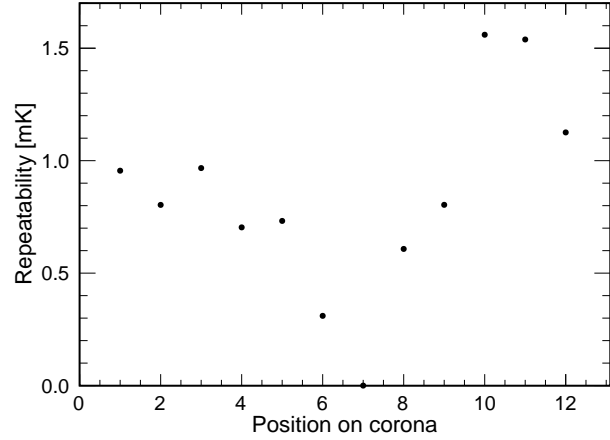


Figure 20: Repeatability as a function of position in the corona for the first set of the LAr-2023 calibration campaign. Sensor in position 7 is taken as reference.

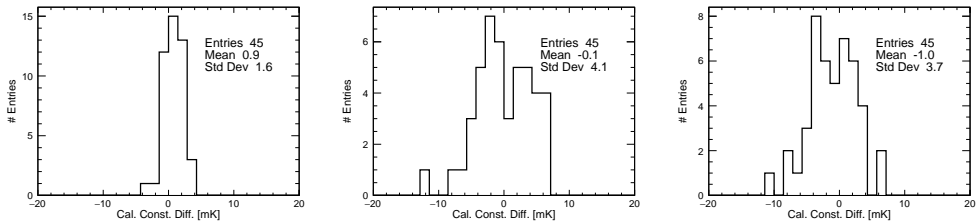


Figure 21: Difference between offsets for two calibrations. Left: LN2-2022 and LN2-2023. Middle: LN2-2022 and LAr-2023. Right: LN2-2023 and LAr-2023.

477 Ageing and long term stability have also been addressed. The left panel of Fig. 21
 478 shows no difference between the offsets calculated in LN2 with a delay of one year. A bet-
 479 ter understanding of this effect is achieved by comparing with the LAr-2018 calibration,
 480 as shown in the next section.

481 *5.4. Comparison between new and old calibrations*

482 Fig. 22 shows the distribution of the offset difference between the LAr-2018 and LAr-
 483 2023 calibrations. The mean of the distribution is -0.1 ± 0.6 mK, excluding any relevant
 484 systematic drift. The standard deviation of the distribution, 4.3 mK, is only slightly
 485 larger than the ones obtained in the comparison between newer calibrations, which could
 486 be due to the unknown contribution of the uncorrected readout offsets, pointing to small
 487 or non-existing ageing effects. This can also be observed in Table 2, summarizing the
 488 results of all possible comparisons between calibration campaigns, showing the mean and
 489 standard deviation of those comparisons. The lowest standard deviation, 1.6 mK, is
 490 obtained for the LN2-2022 to LN2-2023 combination, which is somehow expected since
 491 i) the cryogenic liquid is the same, ii) ageing should be small since there is only one year
 492 difference and iii) having use the same readout channels, readout offsets cancel out.

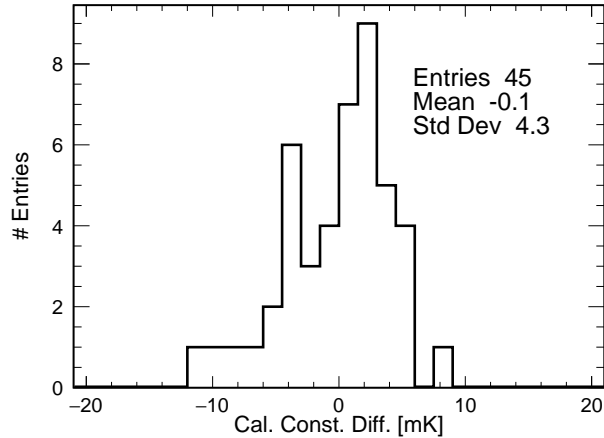


Figure 22: Difference between offsets for LAr-2018 and LAr-2023 calibration campaigns.

493 The difference between the constants obtained in two calibration campaigns can be used
 494 to estimate the total calibration error. Since ProtoDUNE Horizontal Drift (ProtoDUNE-
 495 HD), the next iteration of the ProtoDUNE-SP detector, and DUNE will use LAr, the

	LAr-2018	LN2-2022	LN2-2023	LAr-2023
LAr-2018	-	0.0, 3.5	0.9, 3.9	-0.1, 4.3
LN2-2022	-	-	0.9, 1.6	-0.1, 4.1
LN2-2023	-	-	-	-1.0, 3.7
LAr-2023	-	-	-	-

Table 2: Mean and standard deviation of the difference between the calibration constants obtained in two calibration campaigns.

best estimation of the error would come from a LAr to LAr comparison close in time to the actual detector running. Being this combination not available, three other combinations can be used. The comparison between the LN2 calibrations from 2022 and 2023 yields a standard deviation of 1.6 mK, which should represent the quadratic sum of the individual calibration errors. Assuming equal errors for both campaigns, this implies a single calibration error of approximately 1.13 mK. In this case, readout channel offsets cancel out, although real fluctuations in those offsets still contribute to the estimated single calibration error. The comparison between LAr calibrations from 2018 and 2023 provides further insight, with a standard deviation of 4.3 mK, corresponding to a single calibration error of about 3.0 mK. However, this value includes uncorrected readout offsets as well as potential effects from sensor ageing. Finally, comparing the new LAr and LN2 calibration campaigns avoids issues related to readout offsets and ageing but may be affected by the differences in cryogenic liquids. These comparisons yield a similar standard deviation around 3.8 mK, implying a single calibration error of approximately 2.7 mK. This value thus establishes an upper limit on the LAr calibration error. In summary, the individual calibration error in LAr is estimated to lie between 1.6 and 3.0 mK. This range is consistent with an independent estimate of 1.7 mK obtained using a different method for the LAr-2018 calibration (see Sec. 4.3.5).

6. Conclusions

The DUNE experiment will require the construction and operation of the largest cryostats ever used in a particle physics experiment. This makes the continuous measurement of temperature gradients in liquid argon crucial for monitoring the stability of the cryogenics system and for detector calibration. R&D on the calibration of RTD probes started in 2017, leading to promising results for sensors installed in the DUNE prototype at CERN.

520 The first setup proved the viability of the method, obtaining a calibration error of 1.7
521 mK. A key component was the readout electronics, with an intrinsic resolution better
522 than 0.5 mK in the comparison between two channels. The mechanics was also crucial,
523 with several insulation layers consisting of independent concentric volumes, ensuring
524 minimal convection in the inner volume. Sensors were contained in an aluminium capsule,
525 enabling slow cool-down and warm-up processes, found to be fundamental to guarantee
526 the integrity of the sensors and to minimize the effect of ageing.

527 The calibration system was later enhanced to accommodate the large-scale calibration
528 required for the DUNE detectors. The capacity of the inner capsule was increased from
529 4 to 14 sensors, while improvements were made to the insulation and symmetry of the
530 system to minimize temperature differences between sensors. The new system has slightly
531 worst repeatability for sensors in the same set, but reduces the statistical and systematic
532 errors associated to the calibration tree, needed to relate any two sensors in different
533 calibration sets. Calibration with the new setup has achieved a precision in the range of
534 1.6-3.0 mK, substantially better than the 5 mK DUNE requirement.

535 Another difference between the new and old calibrations is the use of a different
536 cryogenic liquid. While DUNE will use LAr, LN2 is cheaper, simplifying the process of
537 massive calibration for DUNE detectors. The 10 K difference between those liquids has
538 a minimal effect on the calibration constants.

539 A comparison of the four calibration campaigns has provided valuable insights into
540 aging effects, with no evidence of RTD aging observed over a five-year period. This
541 highlights the stability and reliability of the PT-102-based system.

542 **7. Acknowledgments**

543 The present research has been supported and partially funded by Conselleria d’Innovació,
544 Universitats, Ciència i Societat Digital, by the Fundación ‘La Caixa’, and by MICINN.
545 The authors would also like to thank all the people involved in the installation,
546 commissioning and operation of ProtoDUNE-SP, specially to Stephen Ponders.

547 **References**

- 548 [1] Abi, B., et al. (DUNE), 2017. The Single-Phase ProtoDUNE Technical Design Report
549 [arXiv:1706.07081](https://arxiv.org/abs/1706.07081).

- 550 [2] Abi, B., et al. (DUNE), 2020a. Deep Underground Neutrino Experiment (DUNE), Far Detector
 551 Technical Design Report, Volume I Introduction to DUNE. JINST 15, T08008. doi:10.1088/
 552 1748-0221/15/08/T08008, arXiv:2002.02967.
- 553 [3] Abi, B., et al. (DUNE), 2020b. Deep Underground Neutrino Experiment (DUNE), Far Detector
 554 Technical Design Report, Volume II: DUNE Physics arXiv:2002.03005.
- 555 [4] Abi, B., et al. (DUNE), 2020c. Deep Underground Neutrino Experiment (DUNE), Far Detector
 556 Technical Design Report, Volume IV: Far Detector Single-phase Technology. JINST 15, T08010.
 557 doi:10.1088/1748-0221/15/08/T08010, arXiv:2002.03010.
- 558 [5] Abi, B., et al. (DUNE), 2020d. First results on ProtoDUNE-SP liquid argon time projection
 559 chamber performance from a beam test at the CERN Neutrino Platform. JINST 15, P12004.
 560 doi:10.1088/1748-0221/15/12/P12004, arXiv:2007.06722.
- 561 [6] Abi, B., et al. (DUNE), 2020e. Long-baseline neutrino oscillation physics potential of the DUNE
 562 experiment. Eur. Phys. J. C 80, 978. doi:10.1140/epjc/s10052-020-08456-z, arXiv:2006.16043.
- 563 [7] Abi, B., et al. (DUNE), 2021a. Prospects for beyond the Standard Model physics searches
 564 at the Deep Underground Neutrino Experiment. Eur. Phys. J. C 81, 322. doi:10.1140/epjc/
 565 s10052-021-09007-w, arXiv:2008.12769.
- 566 [8] Abi, B., et al. (DUNE), 2021b. Supernova neutrino burst detection with the Deep Under-
 567 ground Neutrino Experiment. Eur. Phys. J. C 81, 423. doi:10.1140/epjc/s10052-021-09166-w,
 568 arXiv:2008.06647.
- 569 [9] Abud, A.A., et al. (DUNE), 2022. Design, construction and operation of the ProtoDUNE-SP Liquid
 570 Argon TPC. JINST 17, P01005. doi:10.1088/1748-0221/17/01/P01005, arXiv:2108.01902.
- 571 [10] Acciarri, R., et al. (MicroBooNE), 2017. Design and Construction of the MicroBooNE Detector.
 572 JINST 12, P02017. doi:10.1088/1748-0221/12/02/P02017, arXiv:1612.05824.
- 573 [11] Adamowski, M., et al., 2014. The Liquid Argon Purity Demonstrator. JINST 9, P07005. doi:10.
 574 1088/1748-0221/9/07/P07005, arXiv:1403.7236.
- 575 [12] Adams, D.L., et al., 2020. Design and performance of a 35-ton liquid argon time projection chamber
 576 as a prototype for future very large detectors. JINST 15, P03035. doi:10.1088/1748-0221/15/03/
 577 P03035, arXiv:1912.08739.
- 578 [13] Amerio, S., et al. (ICARUS), 2004. Design, construction and tests of the ICARUS T600 detector.
 579 Nucl. Instrum. Meth. A 527, 329–410. doi:10.1016/j.nima.2004.02.044.
- 580 [14] Axon, . Axon custom cables. URL: https://www.axon-cable.com/en/00_home/00_start/00_index.aspx. last visited: 2022-10-01.
- 581 [15] application bulletin, B.B., . Implementation and applications of current sources and current re-
 582 ceivers. URL: <https://www.ti.com/lit/an/sboa046/sboa046.pdf?ts=1712062207089>. last visited:
 583 2024-04-02.
- 584 [16] Chojnacki, E., 2009. A Multiplexed RTD Temperature Map System for Multi-Cell SRF Cavities,
 585 in: SRF2009, p. 232.
- 586 [17] García-Peris, M.A., 2018. ProtoDUNE T-Gradient development and calibration. Master's thesis.
 587 Valencia U. doi:10.2172/1780813.
- 588 [18] Hahn, A., Adamowski, M., Montanari, D., Norris, B., Reichenbacher, J., Rucinski, R., Stewart,
 589 J., Tope, T. (LBNE), 2016. The LBNE 35 Ton Prototype Cryostat, in: 2014 IEEE Nuclear Sci-
 590 ence Symposium and Medical Imaging Conference and 21st Symposium on Room-Temperature
 591 Semiconductor X-ray and Gamma-ray Detectors. doi:10.1109/NSSMIC.2014.7431158.
- 592 [19] Instruments, N., a. Compactrio systems. URL: <https://www.ni.com/es/shop/compactrio.html>.
 593 last visited: 2024-04-02.
- 594 [20] Instruments, N., b. Ni-9238. URL: <https://www.ni.com/es-es/shop/model/ni-9238.html>. last
 595 visited: 2024-04-02.
- 596 [21] LakeShore, . Platinum sensors applications. URL: <https://www.lakeshore.com/products/categories/overview/temperature-products/cryogenic-temperature-sensors/platinum>. last
 597 visited: 2023-05-18.
- 598 [22] Minco, . Resistance thermometry. URL: <https://www.minco.com/wp-content/uploads/Resistance-Thermometry.pdf>. last visited: 2023-05-18.
- 599 [23] Tektronix, . Keithley 2001 digit high performance multimeter. URL: https://download.tek.com/datasheet/1KW-73954-1_2001-2002_DMM_Datasheet_080323.pdf. last visited: 2024-04-02.
- 600 [24] TempSens, . Rtd cables. URL: <https://tempsens.com/catalog/cables-wires/rtd-triad-cables.html>. last visited: 2024-03-15.
- 601 [25] Xiao, Y. (DUNE), 2021. Purity monitoring for ProtoDUNE-SP. J. Phys. Conf. Ser. 2156, 012211.
 602 doi:10.1088/1742-6596/2156/1/012211.